Influence of diameter and scan strategy on the geometrical, microstructural, and mechanical properties of small Inconel 625 L-PBF struts

J. Rodrigues Da Silva [a,b,*], Z. Hamouche [a], A.-L. Helbert [b], T. Baudin [b], F. Coste [a], P. Peyre [a]

[a] PIMM Laboratory, Arts et Métiers Institute of Technology, CNRS, CNAM, HESAM University, 151 Bd de l'Hôpital, Paris 75013, France
[b] ICMMO, University Paris-Saclay, CNRS, 17 Av. des Sciences, Orsay 91190, France

ARTICLE INFO

Keywords:
Laser powder bed fusion
Size-effect
Microstructures
Struts
Metal
Electron backscatter diffraction

ABSTRACT

The geometries, microstructures, and mechanical properties of vertically built Inconel 625 Laser Powder Bed Fusion (L-PBF) struts were investigated in this study. The influence of strut size (between 0.2 mm and 2 mm) and scan strategy was more specifically addressed. As-built struts exhibit satisfactory geometry and porosity rates, whatever the strut size and scan strategy. Classical columnar grains oriented parallel to the build direction (BD) were obtained, with a $< 001 >$ // BD fiber texture only for the smaller struts (0.2 mm to 0.5 mm), due to the formation of a unique circular melt pool on the whole strut surface. At a smaller scale, the influence of the build strategy is also visible on solidification cells, whose average diameter decreases for outside-in strategies and larger hatching area ratios. The tensile strengths and hardness values are lower for the smaller diameter (0.3 mm) struts and for the inside-out strategies, suggesting the important role played by a finer sub-grain structure and a smaller crystallographic texture on the strengthening of Inconel 625 struts.

1. Introduction

Laser Powder Bed Fusion (L-PBF) is a step-by step additive manufacturing technique reaching a real industrial maturity on an increasing range of materials and parts' geometry or size. The correlation between L-PBF process conditions, the resulting intricate thermal history, formed microstructures, and mechanical properties with or without heat treatment is well documented. This interrelation has been addressed on a large range of materials, including solution-strengthened nickel-based alloys such as Inconel 625 [1,2] considered in the current work, and taking into account the influence of heat treatments [3]. However, few systematic studies have considered in detail the formation of microstructures on small L-PBF objects (less than 2 mm width), including possible thermal boundary conditions occurring when the perimeter and associated contour length of the build object becomes non-negligible compared to the sum of hatching vectors.

L-PBF is particularly suitable for small and complex customized parts requiring high precision such as titanium dental prostheses or scaffolds [4]. Small L-PBF struts are also used as unit cells of lightweight lattice structures with high specific strengths and damping properties [5]. On such small parts, of less than a few mm, the size effect may be most important on local solidification conditions and resulting microstructures and mechanical resistance.

Leicht et al. [6] have investigated the influence of rectangular samples' thickness (between 0.2 mm and 3 mm) and build angle on the microstructures and tensile properties of 316 L L-PBF. Using a conventional contour + stripe hatching strategy, with a 67° angle between layers, authors have evidenced a microstructural transition for wall widths ranging from 0.6 mm to 1 mm. Above 1 mm, large columnar grains are oriented, with a dominant $< 110 >$ texture parallel to the build direction (BD). Below 0.6 mm, smaller grains oriented vertically toward the center of the wall were evidenced.

In a related study, Wang et al. [7] considered cylindrical 316 L L-PBF struts with diameters ranging from 0.25 mm to 5 mm. Authors evidenced a distinct crystallographic texture change from $< 110 >$ for larger samples to $< 001 >$ with smaller diameters, attributed to a heat extraction predominantly oriented along the cylinder's height (= BD) as diameter decreased. A similar texture evolution was also shown by Niendorf et al. [8] on Ti-6Al-4V for vertical strut diameters of 0.6 mm to 5 mm. In both cases [8,9], coarser and more oriented grains towards BD

* Correspondence to: 151 Bd de l'Hôpital, Paris 75013, France.
E-mail addresses: julien.rodrigues_da_silva@ensam.eu (J. Rodrigues Da Silva), Zehoua.HAMOUCHE@ensam.eu (Z. Hamouche), anne-laure.helbert@universite-paris-saclay.fr (A.-L. Helbert), thierry.baudin@universite-paris-saclay.fr (T. Baudin), frederic.coste@ensam.eu (F. Coste), patrice.peyre@ensam.eu (P. Peyre).

were observed on the smaller struts, which is contradictory with findings from Leicht et al. [6]. However, scanning strategies were not systematically mentioned in the aforementioned works, complicating direct comparisons between them.

More recently, Carassus et al. [9] also analyzed rectangular 316 L L-PBF samples in the 0.5 mm to 1.5 mm range. A lower density was obtained for the 0.5 mm samples compared to larger ones, contrary to other findings [8,11]. Smaller grains were shown in the external part of the builds, attributed to a single melting-solidification and a higher cooling rate. The change of build angle induced a new crystallographic texture: from a dominant < 001 > fiber texture for a 90° angle (= with the sample oriented parallel to the build direction), to a mix of < 001 > and < 101 > crystal orientations for a 0° angle (sample parallel to the building platform). Other studies also show struts built at different angles [8,11]. For a 45° angle, the microstructures still form parallel to the build direction; however, due to the angle, epitaxy is no longer possible along the entire height of the beams and is interrupted by the edge of the strut.

On 316 L, the reduction of strut diameter also induces the formation of larger subgrain dendrite arm spacings (DAS), attributed to a more intense heat accumulation, and a decrease of hardness and tensile strength due to a reduction of Hall-Petch effect [7]. The occurrence of a decrease in tensile strength with a reduction of the thickness (from 1.5 to 0.5 mm) was confirmed by Carassus et al. [9] along with a higher strain rate sensitivity in the 10^{-3} s^{-1} – 8 s^{-1} range on 316 L L-PBF than on conventionally manufactured 316 L. However, the larger solidification cells observed by Wang et al. [7] on small (D=1 mm and 2 mm) 316 L struts are contradictory with finite element simulations carried out by Promoppatum et al. [12] who demonstrated higher cooling rates for smaller strut diameters. Wang et al. [7] have shown also that the cell diameter is coarser in the outer ring of 1 mm and 2 mm struts, resulting in lower hardness values. Similar hardness results were obtained by Zhang et al. [13] on a 0.35 mm strut in Inconel 718.

The influence of thin-walled L-PBF structures was also addressed by Wróbel et al. [14] on Hastelloy X Nickel. Results indicate that for the thinner walls (~ 0.1 mm width), built with a single L-PBF track, melt pools are larger and shallower compared to thicker walls. Moreover, solidification cells, oriented parallel to the build direction, were coarser close to the edge of the walls, and thinner in the center of the parts. On the same alloy and considering 0.25 mm to 2 mm struts, Sanchez-Mata et al. [15] have shown a single crystal growth in the center of smaller struts. However, it is surprising that the main texture for the smallest struts exhibits a < 110 > // build direction (BD) orientation rather than < 100 > // BD, which contradicts findings from other studies.

To the authors' knowledge, one of the only published works on Inconel 625 struts is by Leary et al. [10], which focuses on possible gas turbine applications and details the tensile properties of Inconel 625 structure lattices. In their preliminary work, authors did not evidence any significant change of density with strut diameter, except for 0.2 mm struts which exhibited lower density levels than larger diameters. Such a limited impact of strut diameter on the density of built material confirms previous findings on 316 L [7]. However, the study did not provide data on build strategies or microstructures.

Regardless of the material used, an open question remains regarding to the high GND dislocation density – around 10^{15} m^{-2} - induced by the L-PBF process [1,16], particularly for small samples of less than 1 mm, and high aspect ratios. For instance, Bertsch et al. [17] showed that the high dislocation densities may result from deformation caused by thermal contraction or expansion in a constrained environment. Increasing the sample size might intensify embedding effects during melt-pool solidification, as melt pools are surrounded by solidified metal, whereas melt pools are mostly surrounded by powder in the smaller struts. However, the size effect on thermally induced hardening and dislocation density is yet to be explored.

Finally, manufacturing small metal struts remains challenging, with limited studies available, especially on Inconel 625. Unlike most papers that varies multiple laser parameters, this study uses simplified experimental conditions, keeping laser power and scan speed constant. This approach allows for a clearer understanding on how the build strategy and strut diameter affect the feasibility, geometric accuracy, microstructures, and mechanical properties of struts in the 0.2 mm to 2 mm range.

Additionally, the origins of microstructures are often understudied and merely attributed to thermal conditions. This paper offers an original perspective by examining the geometry of melt pools and their influence on solidification. Moreover, the research provides a comprehensive link between melt pool geometry, microstructures at various scales—from grains to dislocation density—and their combined influence on macroscopic mechanical properties. This approach provides crucial insights into the engineering of lattice structures primarily composed of small L-PBF struts.

2. Materials and experimental conditions

A gas-atomized Inconel 625 powder supplied by SLM Solutions Group AG was used in this study, whose SEM analysis is shown in Fig. 1. Its chemical composition is given in the Table 1. The grain size distribution was determined with a Cilas Particle Size 920 L analyzer. The following values were obtained: D_{10} = 11 μm, D_{50} = 25 μm, and D_{90} = 42 μm(D_{50} = median diameter of the grain distribution).

L-PBF parts were manufactured with an SLM125 HL industrial machine, using a 400 W output power fiber laser (λ=1.07 μm) from IPG Photonics. The laser beam diameter, measured at the focal distance with an Ophir Spiricon beam analyzer, was 0.06 mm. Additional trials were conducted on a homemade open-architecture L-PBF set-up (so-called MIMAS machine) equipped with high-speed imaging of the melt pools, but with a smaller 50 mm substrate plate. In both cases, the L-PBF process was carried out under an argon atmosphere to prevent oxidation (max O_2% = 400 ppm).

Two kinds of specimens were built: (1) 0.2 mm to 2 mm diameter struts with a 20 mm height, incorporated into a « Parthenon » sample i.e constrained by 2 mm thick plates in their lower and upper part faciliting the analysis of geometries and microstructures; (2) 50 mm-height tensile specimens designed for investigating mechanical strengths under uniaxial tensile loading. All parts were positioned vertically on the substrate plate to align the build direction with the z-axis of the samples, as depicted in Fig. 2.

Each sample was fabricated in five replicates, and all analyses were therefore repeated five times on each replicate.

Following a preliminary L-PBF process optimization, four strategies were carried out on 0.2 mm to 2 mm struts: C_I (Contour inside-out), 1C_H (1 contour + hatching), 3C_H_O (3 contours outside-in + hatching), and 3C_H _I (3 contours inside-out + hatching), with a unique 90 W- 450 $mm.s^{-1}$ condition (for hatching and contour), a 30 μm layer height, and a single vertical build direction (Fig. 3). For these parameters, a single welding bead is 120 μm in width. These strategies, along

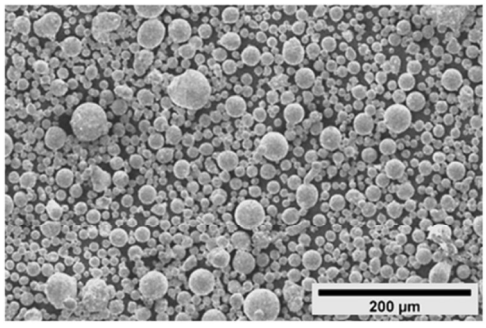

Fig. 1. SEM analysis of the Inconel 625 powder (D_{10} =11 μm, D_{50} = 25 μm, and D_{90} =42 μm).

Table 1
Chemical composition (weight %) of Inconel 625 powder.

Element	Ni	Cr	Fe	Mo	Nb +Ta	Co	Al	Ti	Si, C, Mn, P, S
weight %	Bal.	22.16	0.3	9.20	3.67	0.30	0.17	0.14	$\leq$ 0.05

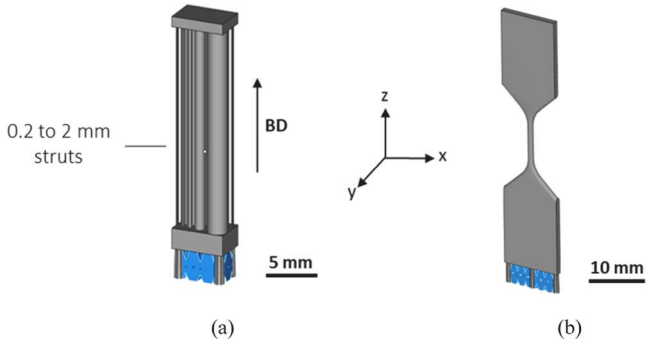

Fig. 2. CAD (Computed Aided Design) geometries of L-PBF samples, (a) Parthenon sample including 0.2 mm to 2 mm vertical struts constrained by 2 mm thick plates in their lower and upper part, (b) tensile specimen (for a 1 mm diameter sample). All parts were positioned vertically on the substrate plate to align the build direction (BD).

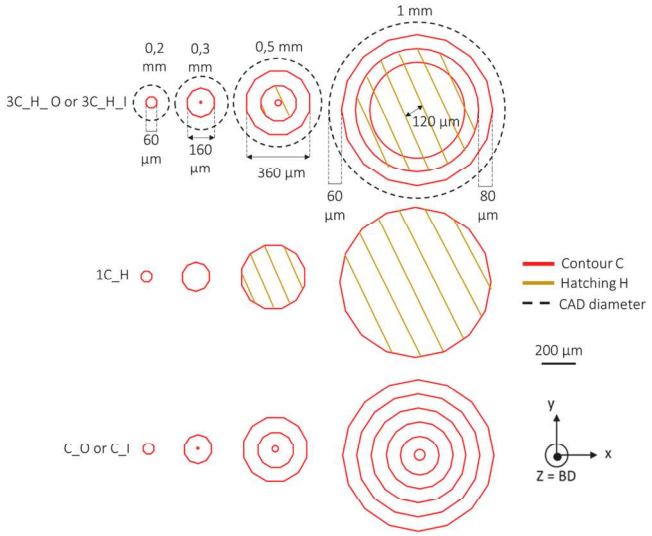

Fig. 3. L-PBF build strategies for struts with diameters ranging from 0.2 mm to 1 mm and their corresponding nomenclature. For the 3C_H strategy, the CAD diameters are also included to illustrate the expected final diameters.

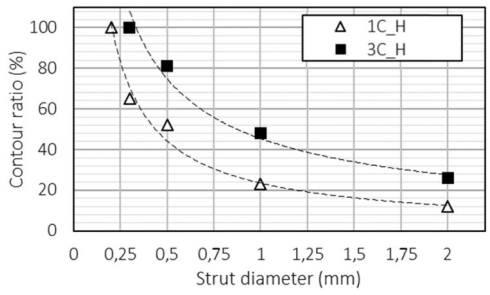

Fig. 4. Contour ratio versus strut diameter for two scan strategies (1C_H: hatching + 1 contour vs 3C_H: Hatching + 3 contours).

with the strut diameters, modified the surface ratio of contours/hatching as shown in Fig. 4. The following parameters were kept constant: hatch distance = 120 µm, contour offset = distance between contour circles= 80 µm, external contour offset (distance between the CAD diameter D and the first contour = 60 µm), and build angle = 16° (angle between hatch lines of layer n and layer n + 1) as recommended by SLM Solutions on Inconel 625.

Geometrical features including roundness ($R = 4S/(\pi . D_{max}^2)$, with S = section (m^2), D_{max} (m^2) = maximum diameter) and experimental equivalent diameter ($D_{eq} = (4S/\pi)^{0.5}$) were estimated on transverse optical micrographs (x, y), and a dedicated Python script.

Microstructures were investigated on transverse (x, y plane) and longitudinal (x, z) plane cross-sections on as-built samples i.e. without subsequent heat treatment. The following metallographic procedure was used: (1) specimens were cold-mounted to avoid deleterious deformation of small built objects, (2) SiC polishing was performed up to the 2400 grade, with 3 µm, 1 µm diamond suspension and 20 min final polishing with colloidal silica (OPS) suspension, (3) cold mounts were dissolved in acetone to carry out Scanning Electron Microscopy (SEM) and Electron Backscatter Diffraction (EBSD) observations.

Strut densification was evaluated via image analysis using ImageJ software, considering longitudinal (x, z) optical micrographs, as statistically more reliable than transverse sections.

SEM observations of solidification microstructures were conducted on a Hitachi 4800 S FEG, following etching of as-polished samples in a 92 % HCl + 5 % H_2SO_4 + 3 % HNO_3 solution for 20–30 s. EBSD analyses were carried out at 20 kV on window sizes equivalent to the strut size (0.2, 0.3, 0.5, 1 mm) or on a quarter of the 2 mm strut. They were obtained on an SEM-FEG Zeiss Sigma, employing a 1 µm step size for conventional Inverse Pole Figures (IPF) and texture analysis, and a 0.1 µm step size for intragrain Kernel Average Misorientations (KAM) and Geometrically Necessary Dislocations (GND). Raw EBSD data were acquired with a Nordif detector indexed + and analyzed with OIM 6.1 software. Dislocation density was also investigated by the analysis of X-ray diffraction (XRD) peak broadening and Williamson-Hall equation [18]. XRD diffractograms were obtained on an X'PERT PANalytical equipped with a cobalt anticathode (λ_{Cu} = 0.179 nm).

To assess the strain evolution in the gage section during tensile tests carried out at 8.10^{-3} s^{-1}, the digital image correlation (DIC) technique was used, with a 29 million Pixels Vieworks camera for image acquisition and the VIC-3D software for data measurement and correlation. Powder particles stuck to the sample surface were used as the main pattern to ensure adequate image quality for DIC analysis.

3. Results

3.1. Geometry and dimensional accuracy

The experimental diameter and the roundness of built samples (Fig. 5) are initially considered. On average, the diameters programmed in the digital file are fairly well respected (less than 10 % difference). However, some differences are noticed. Firstly, the relative deviations (RD) between CAD and the as-built objects decrease as the diameter increase (from +11 % to −4 %). Secondly, the scan order (inside-out I or outside-in O) affects the geometry of objects: I diameters (C_I and 3C_H_I) are systematically larger than O ones (C_O and C_H_O), and get closer to CAD diameters D_{CAD} (Fig. 6). This indicates that optimizing the build strategy allows for minimizing discrepancies between experimental and CAD diameters.

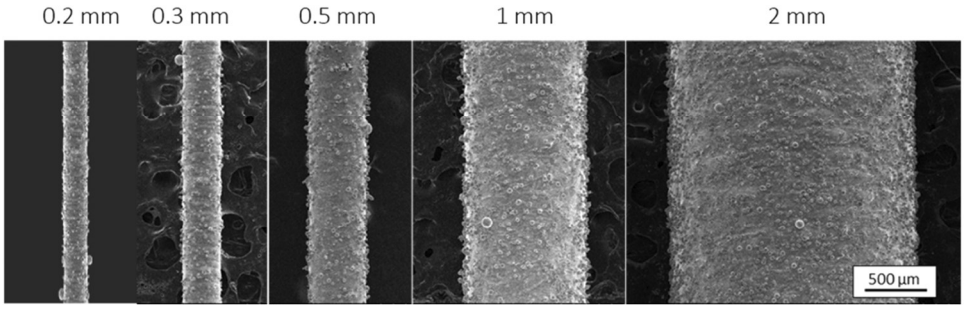

Fig. 5. SEM images of L-PBF-manufactured Inconel 625 strut surfaces with diameters ranging from 0.2 mm to 2 mm using the 3C_H_I strategy.

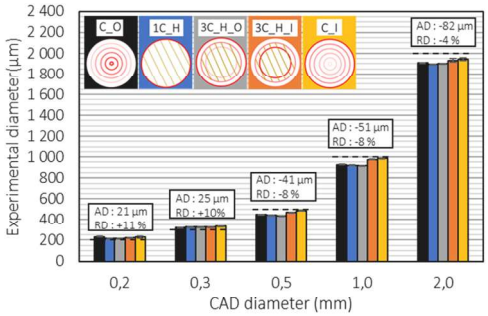

Fig. 6. Experimental diameter versus CAD diameter for L-PBF struts surfaces with diameters ranging from 0.2 mm to 2 mm (AD = Absolute Deviation, RD = Relative Deviation). Error bars represent ± SD from the mean value (n = 5).

The built diameter depends on the width of the external contour vector, which defines the external geometry of the part. Since the distance between the external contour and the theoretical CAD envelope remains constant, I samples are expected to have larger external contours (EC) than O-I samples. This is rather logical considering that for I samples, the EC is the last fusion contour, preheated by previous ones, whereas, for O struts, the EC is carried out first, with more powder dragging (denudation) [19]. This contributes to a stronger thermal dissipation and limits track width.

The roundness parameter is smaller for 0.2 mm and 0.3 diameters but remains above 0.9 for all the observed struts (Fig. 7). However, there is no clear and reliable modification of roundness with the scan strategy. Surprisingly, a large scatter is shown for D= 0.2 mm where a single contour was carried out, regardless of the build strategy (Fig. 3). This scatter could result from the instability of the single melt-pool observed with high-speed imaging for D 0.2 mm and D = 0.3 mm diameters. For larger diameters (1 mm and 2 mm), the roundness exceeds 0.98, as small melt-pools accurately follow the CAD file contour

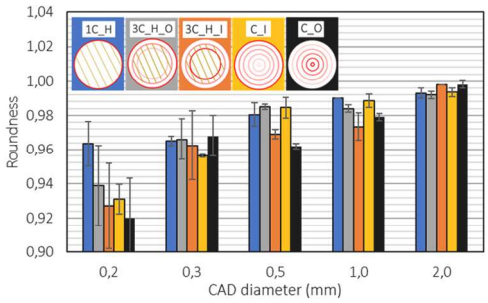

Fig. 7. Roundness of L-PBF struts with diameters ranging from 0.2 mm to 2 mm using five different scan strategies (roundness: $R = 4S/(\pi \cdot D_{max}{}^2)$). Overall, the roundness is satisfactory, approximately 0.98, except for the smallest struts. Error bars represent ± SD from the mean value (n = 5).

3.2. Microstructures

The densification of struts was initially assessed for various build strategies and diameters. With the exception of one strategy (3C_H_O), and the smaller diameter of D = 0.2 mm, porosity consistently remains below 0.6 %. It decreases even further to below 0.25 % for 1 mm and 2 mm diameters regardless of the build strategy (Fig. 8). This reduction in porosity with strut diameter disagrees with results reported by Leary et al. [10] who observed lower porosity (0.02 %) for smaller struts. On longitudinal cross-sections, the occurrence of rather large pores (70 µm) are clearly shown on 0.3 mm and 0.5 mm struts with the 3C_H_O strategy. These pores are aligned vertically, globally positioned at the interface between contours and hatching areas, resembling keyhole pores (Fig. 9). This keyholing effect should be one explanation for the observed results and may be promoted by short hatch vectors that increase local preheating effects, and penetration depths. Interestingly, this building strategy (3C_H_O), which results in a higher pore count, is usually recommended for building structure lattices and supporting structures. Apart from 3C_H_O, other build strategies did not exhibit a distinguishable effect on porosity.

EBSD was then conducted on transverse and longitudinal cross-sections to analyze grain distributions and crystallographic textures. Typically, L-PBF microstructures are formed during a high cooling rate solidification (usually between 10^5 K.s^{-1} and 10^6 K.s^{-1} [14]), resulting in fine structures predominantly oriented towards the build direction. For small samples, with a high surface/volume ratio, the border strategy may significantly impact the whole built material, and the thermal isolation of the material surrounded by the powder bed [20] could play a non-negligible role on local microstructures.

The influence of strut diameter is highlighted in Fig. 10 for a 3C_H_O strategy and transverse cross-sections (x, y plane). A dominant < 001 > grain orientation along the build direction, corresponding to a < 001 > fiber texture, is evident for smaller diameters of 0.2 mm and 0.3 mm, leading to a strong anisotropy. As the strut diameter increases,

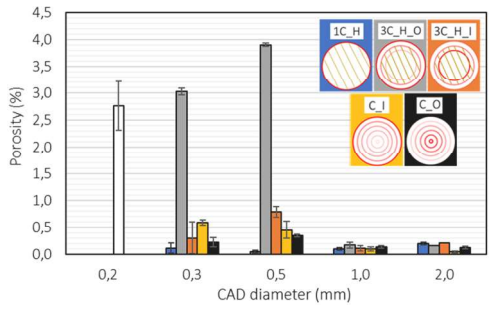

Fig. 8. Porosity (surface %) on longitudinal cross-sections for L-PBF struts with diameters ranging from 0.2 mm to 2 mm and using five different scan strategies. For the 0.2 mm struts all scan strategies are identical (only one contour), so only one strategy is presented. Error bars represent ± SD from the mean value (n = 5).

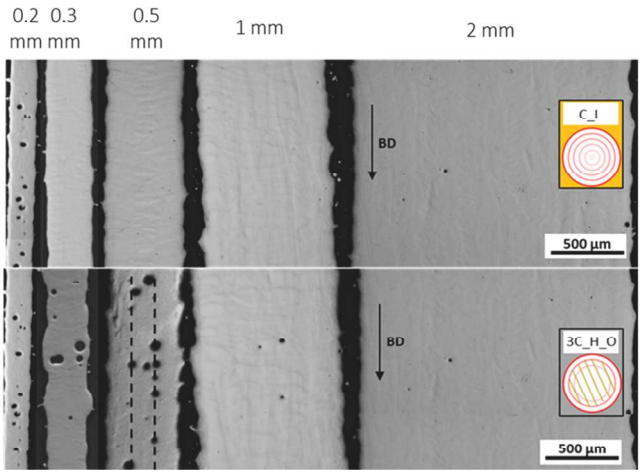

Fig. 9. Optical micrographs of longitudinal sections (parallel to the BD) of L-PBF struts with diameters ranging from 0.2 mm to 2 mm for C_I (up) and 3C_H_O (down) scan strategies. Dotted lines indicate the interface between hatching and contour areas.

the fiber texture becomes more diffused, and globally reduced, with texture intensities of less than 3. This result aligns with previous works on 316 L struts [7]. However, current results on Inconel 625 do not exhibit a transition to < 110 > orientation for large struts as proposed by Wang et al., but instead exhibit randomly distributed and oriented grains.

The occurrence of a strong < 001 > texture along the build direction can be directly related to the melt-pool bottom curvature i.e. the inclination of the solid-liquid interface versus BD. For small diameters, a single melt-pool is formed, with a rather planar melt-pool interface, whereas larger struts exhibit a larger melt-pool curvature due to a 3D thermal dissipation, consistent with conclusions by [7]. Basically, < 001 > is also the preferred growth direction for FCC alloys according to usual solidification theories. This implies that, for small struts, FCC grains tend to align their < 001 > growth along the main thermal gradient direction, parallel to the build direction. This size-dependent texture mechanism will be detailed in the discussion section.

Build strategy effects were also shown (Fig. 11), except for the smaller struts (0.2 mm and 0.3 mm), which all correspond to a one single contour strategy. For a deeper insight into these strategy and size effects, the average grain size was determined on cross-sections using the equivalent diameter method, where each grain was equated to a circle of diameter D_{eq}. However, the size of the grains varied significantly (from 10 to 100 µm) between areas, leading to differences in diameter dispersion. Thus, to reduce these standard deviations, the grain sizes were calculated on three distinct areas as defined below:

- The first outer ring (OR) is the area at the interface between the processed part and the powder (Fig. 12a). It is represented by equiaxed grains of small size (10–15 µm), regardless of the build strategy, and mostly oriented < 001 > //BD.
- The second inner ring (IR) is the « dartboard » area defined by the contours, with larger and rectangular grains oriented towards the center of the beam. For the C_I strategy, this area occupies the whole strut section. Grain size increases with strut diameter (Fig. 12b), between 30 and 40 µm (0.2 mm and 0.3 mm diameters) and 80–120 µm (D=2 mm). Interestingly, the 1C_H strategy, which emphasizes hatching (Fig. 4) and limits contouring areas to a single track width, induces smaller grain diameter (48 µm) than the other three strategies for D= 0.5 mm, 1 mm, and 2 mm. Additionally, larger grains are also observed in the inner ring with the 3C_H_I (inside-out) strategy compared to the 3C_H_O (outside-in strategy).
- The hatching area (HA) is defined by the hatching vectors (Fig. 12a). It is always located at the center of IPF maps, but may be absent, especially for beams smaller than 0.5 mm in diameter and with the pure contouring strategy CI. Grain size in the hatching area tends to be notably smaller (20–30 µm) than in the IR area. This distinction is particularly noticeable for the 2 mm strut diameter built with the C_H strategy as depicted in Fig. 11. In summary, these grain sizes indicate a clear distinction between relatively small grains formed by a hatching mode i.e. by overlaps of parallel linear tracks in the center of the struts, and larger grains in the contour area, mainly located in the inner ring, near the struts edge.

When considered on longitudinal (x, z) cross-sections, a columnar polycrystalline structure oriented parallel to the build direction is logically shown, in agreement with most of the published works on Inconel 625 or 316 L. The < 100 > // BD texture is confirmed on small diameters (Fig. 13a). However this differs from the results on Hastelloy X [15], where a single crystal is formed at the center of the smaller struts (0.2 mm – 0.3 mm in diameter), but with a < 110 > // BD texture.

In the area at the edge of large strut samples, thin and highly elongated grains are visible, with a β angle of less than 10° versus the build direction (Fig. 13b-d). These high aspect ratio columnar grains are located in the outer ring and correspond to the small equiaxed grains observed in the transverse sections (Fig. 10). They germinate in contact with the powder grains surrounding the struts and progressively reorientate along BD during their growth. They are only formed by a fusion-solidification event and were not remelted by subsequent contour tracks.

In the inner ring of large struts, large columnar grains are visible (Fig. 13b,c), with a predominancy of a < 110 > orientation. The height and width of these columnar grains traduce a strong vertical and lateral epitaxy, promoted by the contour strategy where melt-pools are always aligned, superposed, and juxtaposed similarly. One critical consideration when conducting a metallographic analysis on a longitudinal cross-section of thin struts is the precise positioning of the cut line: if the cut is not exactly positioned at the mid-diameter, the orientation of scan tracks may differ from expectations. This is particularly true for small struts and contour areas.

In the hatching area, due to the rotation angle of 16° between layers inducing a vertical misalignment of fusion tracks, the microstructures analysis is more complex. While there is no evidence of a clear crystallographic texture, a morphological texture is still observed, with smaller grains oriented vertically.

At a finer scale, the size of the sub-grain cellular structure was investigated on SEM micrographs, revealing larger cells for smaller diameter and inside-out strategies C_I and 3C_H_I (Fig. 14). In both cases, this should be attributed to reduced cooling rates near the solidification front, promoting longer growth durations. Based on these data, an estimation of cooling rates V_c ($K.s^{-1}$) is possible using the following equation: $D_{cell} = 50.V_c^{-0.33}$ mentioned by Li et al. [21] for Inconel 625. Cooling rates comprised between $5.8.10^5$ $K.s^{-1}$ (D_{cell}=0.6 µm) and 3.10^4 $K.s^{-1}$ (D_{cell}=1.6 µm) were estimated. Additionally, for larger struts (1 mm and 2 mm), SEM analysis also revealed smaller cells near the outer ring than in the center of the struts. This last result on Inconel 625 contradicts the results of Wang et al. [7] on 316 L who obtained larger cells near the struts edges. IPF maps on transverse sections were also used at a high resolution of 0.05 µm to estimate intercell misorientations showing average misorientation angles ranging from 0.6° to 1.5° regardless of the strut diameters and build strategies.

3.3. Analysis of dislocation density

The estimation of dislocation density was conducted using both X-ray diffraction and EBSD, through the analysis of Kernel Average Misorientations (KAM) within FCC grains.

Initially, an approach based on Williamson–Hall (WH) analysis, introduced by Williamson and Hall in 1953, was employed. This method

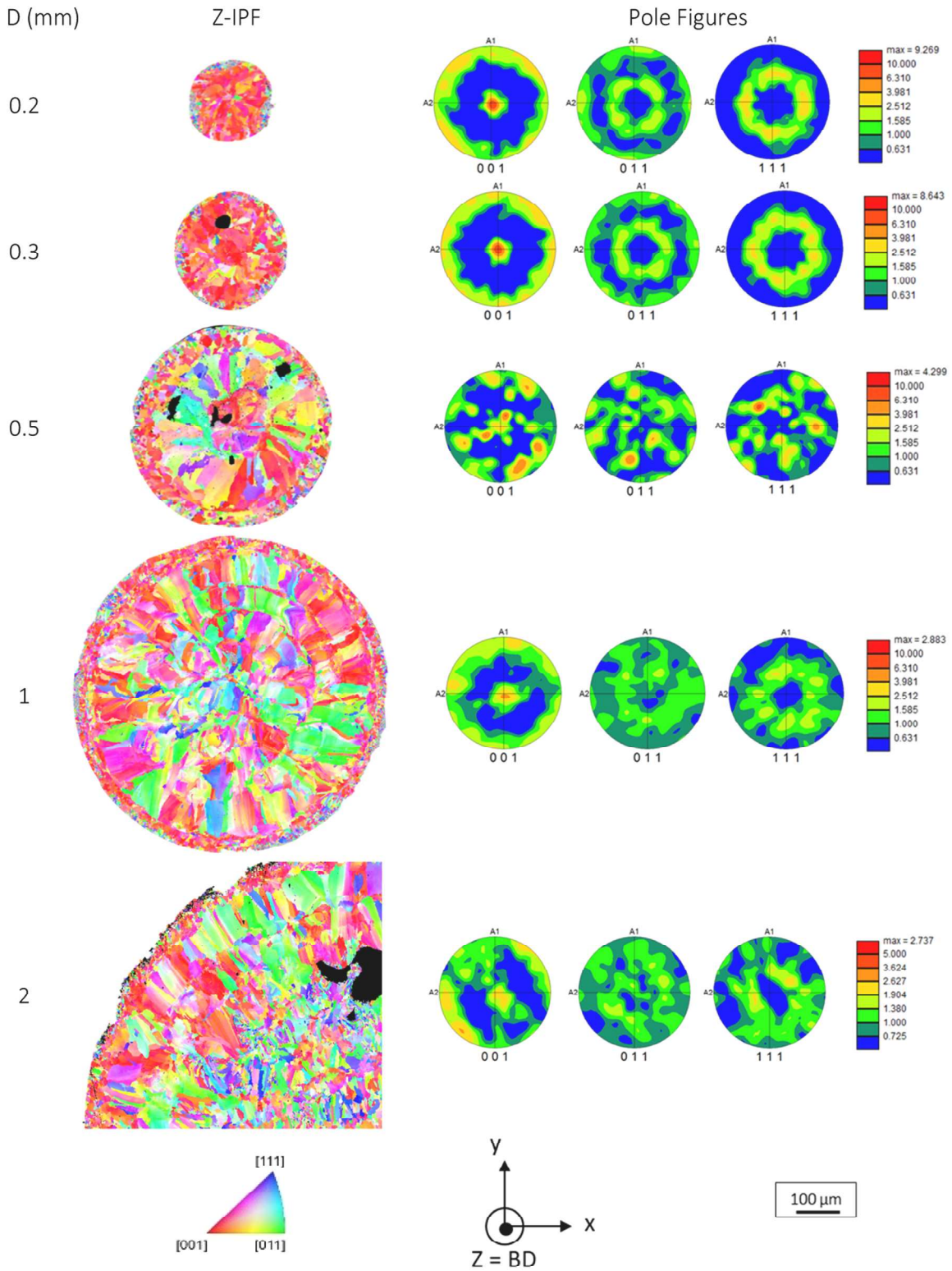

Fig. 10. Inverse Pole Figures (Z-IPF) orientation maps and corresponding Pole Figures (PF) of transverse cross sections of struts with diameters ranging from 0.2 mm to 2 mm built with the 3C_H_O strategy. A more pronounced < 001 > texture // BD aligned with the build direction is observed in the smaller struts.

involved analyzing X-ray peak broadening for various {hkl} planes. Subsequently, a modified version of the Williamson–Hall approach, proposed by Ungár et al. in 1999, was utilized. This modified approach incorporates specific contrast factors (Chkl) for each diffracting plane to account for dislocation slip and strain-induced anisotropy.

The corresponding equation is shown here below (Eq.1), and the slope of the $\Delta K = f(K.\ C_{hkl}^{0.5})$ regression curve (with $K\ (m^{-1}) = 4\ \sin\theta/\lambda$ and $\Delta K\ (m^{-1}) = FWHM.\ \cos\theta/\lambda$) provides an estimation of crystal distortion $\tilde{\varepsilon}$. From this crystal distortion, the estimation of dislocation density $\rho_d\ (m^{-2})$ can be estimated using the Williamson-Smallman [22] equation (Eq.2).

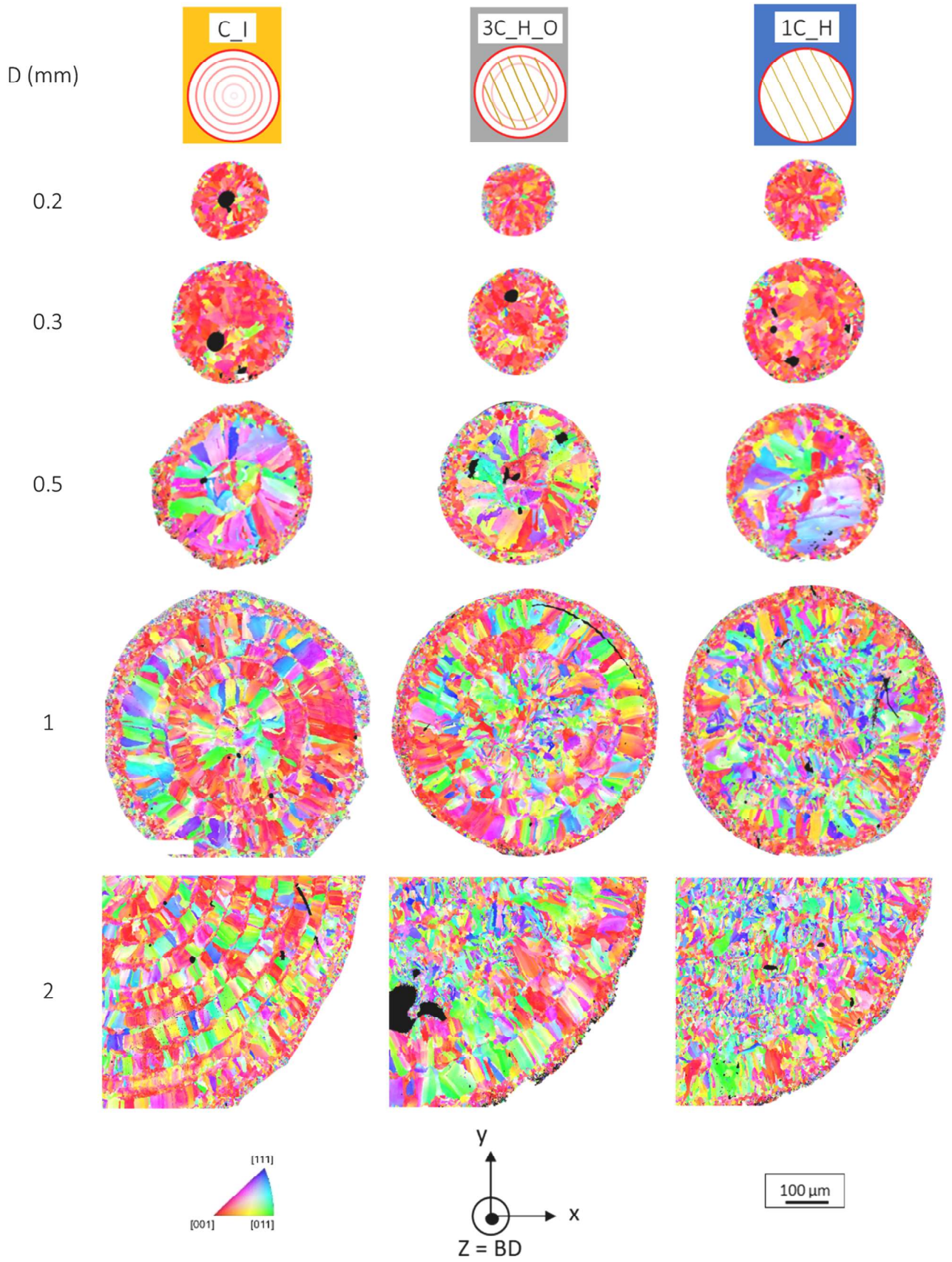

Fig. 11. Z-IPF maps for struts with diameters ranging from 0.2 mm to 2 mm manufactured using three build strategies (C_I, 3C_H_O, 1C_H).

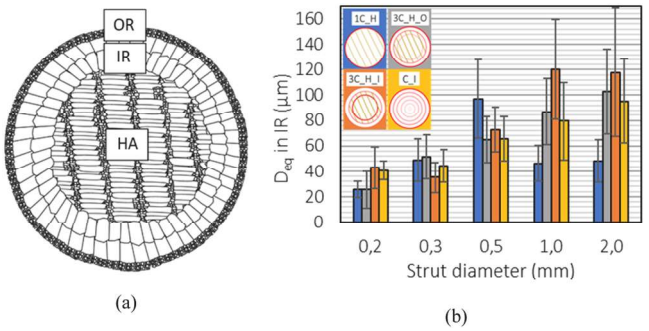

Fig. 12. (a) Diagram of different areas on a transverse cross-section of a built strut (OR: Outer ring, IR: Inner ring and HA: Hatching), (b) equivalent grain diameter in the internal ring. Error bars represent ± SD from the mean value (n = 5).

$$\Delta K = \frac{0.9}{D_s} + \tilde{\varepsilon}.C_{hkl}^{0.5}.K \quad (1)$$

$$\rho_d = \frac{16.1\tilde{\varepsilon}^2}{b^2} \quad (2)$$

Where FWHM (rad) = full width at half maximum of {hkl} peaks, θ (rad) = Bragg diffraction angle, D_s = size of diffracting crystallites (Å), λ = wavelength of anticathode (1.79 Å), C_{hkl} = Contrast Factors (estimated as follows: 0.14 for {111}, 0.21 for {200}, 0.495 for {220} and 0.4 for {311} considering 50 % screw dislocations and 50 % edge dislocations), b = burgers vector of FCC Inconel 625 (= 2,54 Å).

The analysis of $\Delta K = f(K.C_{hkl}^{0.5})$ points provided satisfactory results as the intercept of the three regression lines, directly dependent on diffracting crystallites, was logically the same, and regression coefficients ranging from 0.65 to 0.97 (Fig. 15). However, the calculation of ρ_d values (Eq.2) from the slopes of the three regression lines did not evidence significant differences between the three diameters: $2.28.10^{15}$ m^{-2} (D=0.5 mm), $2.3.10^{15}$ m^{-2} (D=1 mm) and $1.97.10^{15}$ m^{-2} (D=2 mm). This suggest that larger embedding effects in large struts did not play a significant role in the mechanisms of dislocation generation, contrary to the finding of Bertsch et al. [17]. However, the estimation of ρ_d could not be done on 0.3 mm struts, due to the need to juxtapose a large number of struts to reach a sufficient diffracting surface.

Geometrically Necessary Dislocations (GND) were also estimated using KAM determinations. In the center of struts, lower average dislocation densities ρ_{GND} were obtained: $2.28.10^{15}$ m^{-2} (D= 0.5 mm), $1.22.10^{15}$ m^{-2} (D=1 mm), and $1.01.10^{15}$ m^{-2} (D=2 mm). Such a result is rather logical because, in the KAM analysis, only GND are considered whereas the X-ray peak broadening is sensitive to all dislocations, including statistically stored dislocations (SSD). A summary of obtained results is shown in Fig. 16.

Overall, the results did not reveal a significant effect of strut diameter and build strategy on dislocations, whose density remained close to $10^{15}m^{-2}$, under all struts and build conditions.

3.4. Mechanical properties

Vickers Hardness tests (Fig. 17a) and tensile tests were conducted to analyze mechanical behavior at both local and global scales. Hardness values ranged between 260 and 300 $HV_{0.05}$, is consistent with other data from the literature on as-built Inconel 625 [23]. Two key aspects emerge: (1)hardness tends to increase with strut diameter, and (2) 1C_H

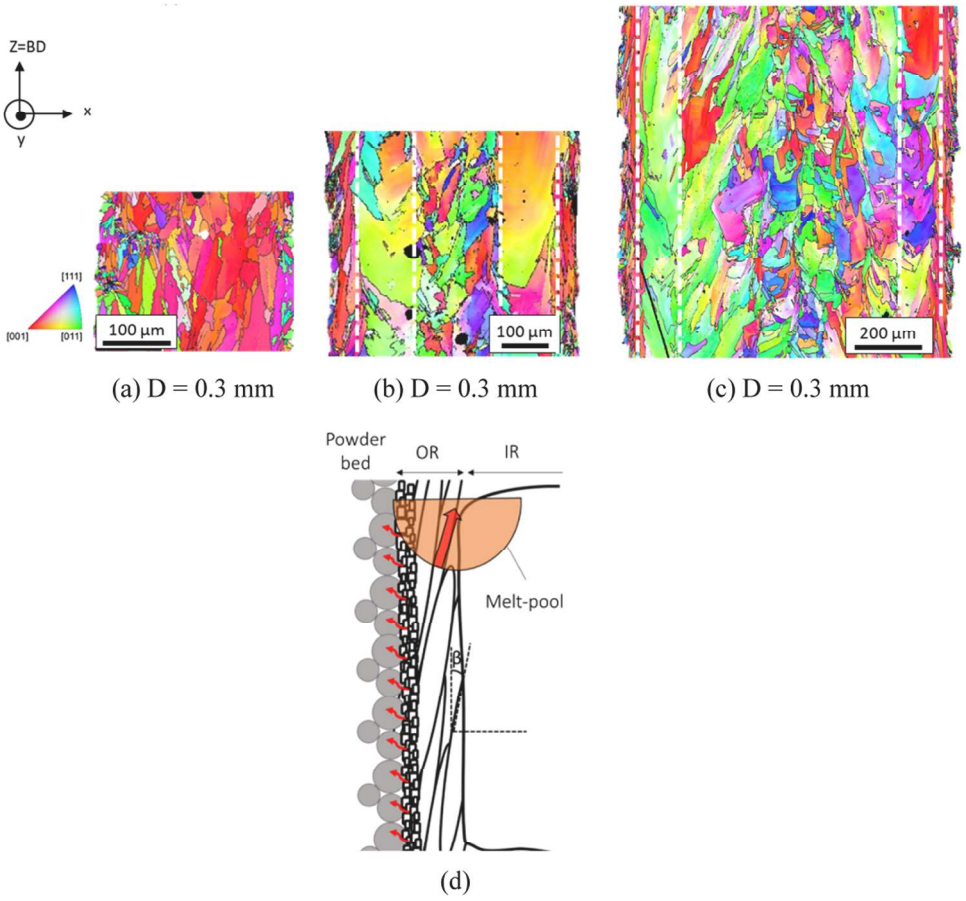

Fig. 13. IPF maps of longitudinal cross-sections of built struts: (a) 0.3 mm diameter, (b) 0.5 mm diameter, (c) 1 mm diameter, using the 3C_H_O strategy (dotted vertical lines indicate the boundaries of the inner ring area) and (d) a diagram showing grain organization in the outer ring based on the shape of the melt pool.

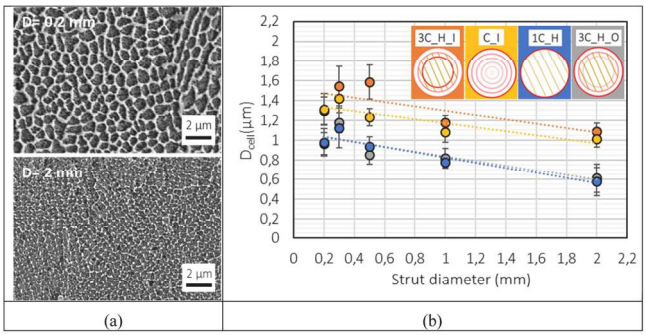

Fig. 14. cellular sub-grain microstructure for (a) 0.2 mm and 2 mm struts (3C_H_O strategy) and (b) the equivalent cell diameter (or cell arm spacing) versus strut diameter ranging from 0.2 mm to 2 mm, with four different scan strategies. Error bars represent ± SD from the mean value (n = 5).

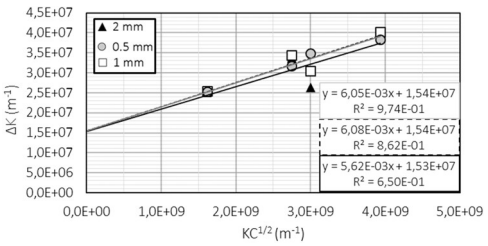

Fig. 15. Modified Williamson-Hall regressions for D= 0.5 mm, D = 1 mm and D= 2 mm struts (3C_H_O strategy).

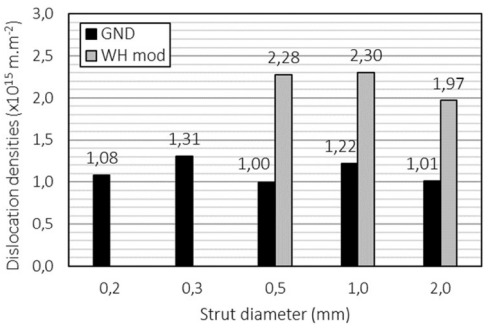

Fig. 16. Dislocation densities obtained with KAM analysis (GND) or Williamson-Hall (WH) and modified Williamson-Hall (WH mod) apporaches for struts with diameters ranging from 0.2 mm to 2 mm (3C_H_O strategy).

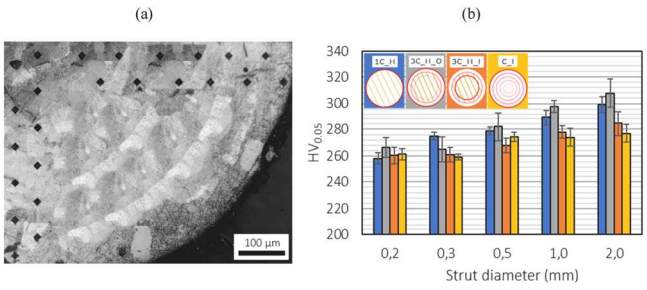

Fig. 17. Microhardness tests (50 g load): (a) an example of a micrograph of indented strut surface and (b) the influence of strut diameter and build strategy on hardness for struts ranging from 0.2 mm to 2 mm in diameter. Outside-In strategies (shown in blue and gray) exhibit better hardness compared to the Inside-Out strategy (shown in orange and yellow). Error bars represent ± SD from the mean value (n = 5).

and 3C_H_O strategies exhibit higher average hardness values, especially for the larger strut diameters (Fig. 17b). This last correlation aligns with the smaller cell diameters observed with 1C_H and 3C_H_O strategies (Fig. 14b), suggesting a Hall-Petch mechanism at play.

Tensile tests also evidenced disparities among the as-built struts. Firstly, in full agreement with Hardness tests, build strategies influence mechanical strengths, with 1C_H and 3C_H_O specimens exhibiting higher resistance (up to 1050 MPa UTS: Fig. 18) than 3C_H_I and C_I specimens. This also confirms that inside-out strategies tend to reduce the mechanical resistance of struts. Secondly, the smaller strut diameter investigated (0.3 mm) has a 35–45 % lower mechanical strength compared to the larger diameters (Fig. 19). For instance, yield strength ($Rp_{0.2}$) ranged between 420 MPa and 500 MPa for D= 0.3 mm, whereas it varied between 600 MPa and 850 MPa for the other diameters (Fig. 19a). Similarly, ultimate tensile strength (R_m) values ranged between 640 MPa and 755 MPa for D= 0.3 mm and between 830 MPa and 1120 MPa for the larger struts (Fig. 19b). This result is rather independent of the larger pore content observed in small struts. To investigate this aspect, an attempt was made to correct the mechanical strengths of small struts by subtracting the surface ratio of pores observed in fracture surfaces from the initial cross-sectional area (Fig. 20). Despite variations in build strategy, surface ratios between 3 % and 12 % were observed, which had a limited influence on corrected results. As a reminder, all programmed build strategies are similar for the D= 0.3 mm struts and involving a single contour track.

The true stress-strain curves were calculated to evaluate the work-hardening behavior of the struts, using Hollomon's strain-hardening equation ($\sigma = k_O\varepsilon_p^n$) in the uniform plastic deformation stage. In agreement with the results by Liang et al. [24], three stages were identified: (1)transition from elastic to plastic for $\varepsilon_p < 4$ %, (2) intermediary regime between 4 % and 10 %, (3) stable plastic flow above $\varepsilon_p = 10$ %). The strain hardening rate $d\sigma/d\varepsilon$ versus true stress in a logarithmic scale (Fig. 21)[25] exhibited a constant decrease with plastic deformation, sharper in the initial stage and slowing down in subsequent stages. These transitions between the different hardening stages should correspond to the microstructure evolution during deformation. The estimated k_0 and n values of the Hollomon equation in the last stable plastic regime are shown in Table 2. For D = 1 mm and 2 mm, n exponents were near 0.24 while for smaller diameters, they ranged around 0.3–0.35. Comparing with De Terris et al. [1] values obtained on a recrystallized Inconel 625 (n = 0.44) suggests lower work-hardenability for the two larger struts, possibly due to their higher initial dislocation density and work-hardening level.

4. Discussion

4.1. Formation of microstructures-Influence of melt-pools

A deeper insight into microstructures requires considering the influence of melt-pool shapes and dimensions on texture formation. This

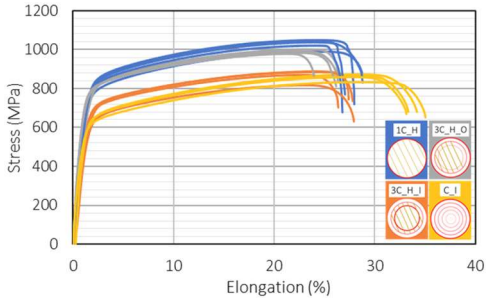

Fig. 18. Conventional tensile curves for a 1 mm strut. Outside-In strategies (shown in blue and gray) demonstrate better mechanical properties compared to the Inside-Out strategy (shown in orange and yellow).

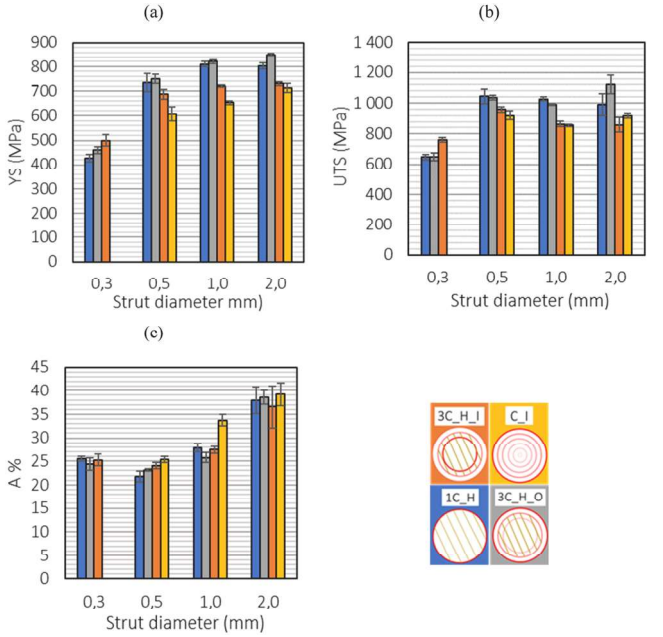

Fig. 19. Tensile properties for struts with diameters ranging from 0.2 mm to 2 mm and four build strategies: (a) Yield strength at 0.2 % elongation, (b) Ultimate tensile strength, and (c) elongation to failure. Error bars represent ± SD from the mean value (n = 5).

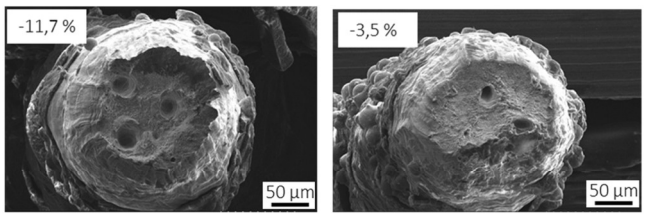

Fig. 20. SEM observations of two fracture surface of a 0.3 mm strut, with corresponding open pore ratios (3C_H_I strategy).

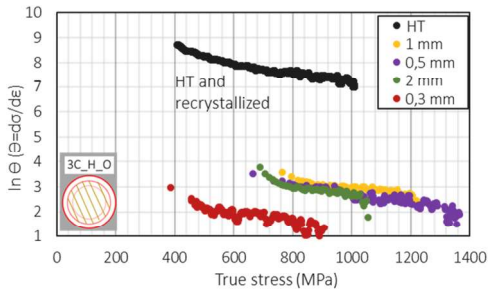

Fig. 21. Strain hardening rate (logarithmic scale) versus true stress for 0.2 mm to 2 mm diameter struts using the 3C_H_O strategy, compared with a recrystallized Inconel 625 sample.

can either be obtained by analyzing the last built layer, which is not remelted by subsequent fusion tracks, by having a closer look at the FCC lattice orientation on IPF maps, or by providing real-time monitoring of the melt pool using a high-speed camera. One assumption concerns the transition from a single static circular melt-pool droplet for small struts, to classical moving L-PBF melt-pools for larger struts with this transition expected for D= 0.5 mm.

For D= 0.3 mm, FCC lattices are consistently oriented towards the center of the strut (Fig. 22). This indicates a circular solidification front

Table 2
Strain hardening exponent (n) and strength coefficient (k_0) in the 10–20 % plastic deformation range for various strut diameters and build strategies.

	3C_H_O		3C_H_I		1C_H	
	n (10–20 %)	k_0 (MPa)	n (10–20 %)	k_0 (MPa)	n (10–20 %)	k_0 (MPa)
0.3 mm	0.38	250	0.35	348	0.34	273
0.5 mm	0.3	513	0.33	414	0.28	520
1 mm	0.24	591	0.24	498	0.24	591
2 mm	0.24	518	0.24	505	0.24	581

Inconel 625 recrystallized: n = 0.44 et k_0 = 239 MPa

growing towards the center of the strut, with a corresponding round melt pool occupying the whole strut surface. Such lattice orientations spanning from 0° to 360°, aids in understanding the fiber texture obtained on small struts (Fig. 10). In-situ melt pool monitoring and FE modeling [26] further confirmed these finding. Interestingly, analysis of FCC lattices on a 1 mm strut reveals a similar orientation of towards the strut center during a contouring path (Fig. 23). The analysis of the top of a 2 mm strut on a longitudinal cross-section indicates that, with an outside-in strategy, small (150 µm) and overlapped melt-pools shape the microstructure at the strut's edge, while a larger (500 µm) circular melt-pool induces a modified microstructure at the center of the strut (Fig. 24). These two examples highlight the direct influence of melt-pool shapes and curvatures on the final microstructures.

Fig. 13b,c illustrates small and high aspect ratio grains, inclined at an β angle versus BD near the strut edge. To understand further this effect, a comparison was made for similar struts and strategies, but between two distinct laser energies P/V (J/m) of 200 J/m (90 W / 0.45 m/s) and 666 J/m (300 W – 0.45 m/s) corresponding to a keyhole mode. A notable change in angle was observed (180-β = 50° vs 15° angle from horizontal), attributed directly to the curvature of the melt-pool, more vertical for the deeper penetrated track (Fig. 25). This confirms the overall influence of the melt-pool shape on final microstructures, especially when laser tracks are vertically aligned, such as contour tracks.

For all the contour areas of struts where scan tracks are vertically and horizontally aligned, aside from the external ring mentioned earlier, well-aligned columnar grains are shown. According to Sofinowski et al. [27], akin to parallel L-PBF tracks without rotating angle, their crystal orientation should be < 011 > // BD, and < 001 > //(O,y), with (O,y) axis parallel to the scan direction and perpendicular to the longitudinal section. However, this texture is directly linked to the average angle of the solidification front versus build direction in the lower part of melt pools i.e. in the non-remelted areas located between the melt pool bottom z-position z_0 and $z_0+\Delta h$ with Δh = layer height. This average melt-pool bottom angle also depends on the hatch distance: the lower the hatch distance, the closer from a < 001 > //BD texture. In that case, and since the FCC lattice logically orientates their (001) plane parallel to

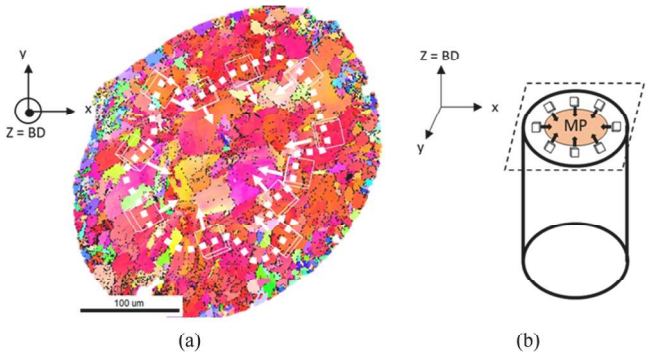

Fig. 22. Orientation of FCC lattices: (a) on a transverse cross-section Z-IPF (D=0.3 mm) and (b) the corresponding diagram on the 3D strut with a schematic melt pool.

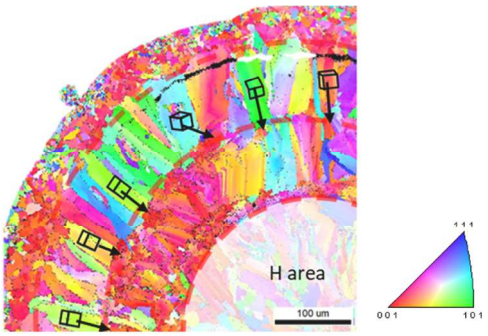

Fig. 23. Orientation of FCC lattices on a Z-IPF map of a transverse cross-section of a 1 mm strut (3C_H_O strategy).

the solidification front (Fig. 26a) in agreement with the solidification theory, the FCC lattice is aligned perpendicular (and parallel) to BD. For larger hatch distances, an average θ= 45° MP bottom angle is obtained. In that case, the FCC crystal still orientates its $< 001 >$ direction perpendicular to the solidification front resulting in a $< 110 >$ //BD texture. For most of the conditions, a $< 001 > + < 110 >$ hybrid texture is obtained (Fig. 26), corresponding to the alignment of grains with the MP edge or MP bottom.

4.2. Contributions to strengthening

Following the recent work by Liang et al. [24], an estimation of the different contributions to the strengthening of Inconel 625 struts is possible using analytical expressions. These contributions are summarized in (Eq.3) and have been estimated for all strut diameters and build strategies. In this equation, we have disregarded the influence of Orowan-like precipitation strengthening [28], assumed to be limited on as-built samples obtained with a high cooling rate solidification.

$$\sigma_y = \sigma_{SS} + \sigma_G + \sigma_{dis} + \sigma_C \quad (3)$$

With σ_{ss} = solid solution strengthening, σ_G = grain boundary strengthening, σ_{dis} = dislocation strengthening, and σ_C = solidification cell boundary strengthening

- Solid solution strengthening

The estimation of solid solution strengthening and its dependency on alloying elements can be expressed using Eq.4 [29] where Mo and Nb/Ta refractory elements are the primary contributors to sol-sol strengthening. A constant σ_{ss} = 355 MPa contribution is obtained for all build conditions and strut diameters.

$$\sigma_{ss} = \left(\sum_i k_i^2 . C_i \right)^{0.5} \quad (4)$$

With

C_i the atomic fraction of i-element and k_i a solid solution strengthening constant for i-element (Table 3)

- Dislocation-induced strengthening

The contribution of dislocation to strengthening is classically described by the Taylor equation (Eq.5). However, contrary to Liang et al. [24], ρ_0 values were not estimated by x-ray diffraction (~ 2. 10^{15} m^{-2} in Fig. 16), but instead by the dislocation density at the core of solidification cells, assumed to be close to that of the as-recrystallized samples (~4.10^{13} m^{-2} according to Joshi et al. [31] on a Ni20Cr alloy). Considering the differences in Taylor factors (M=2.6 for the small struts oriented <001 > and 2.9 for the larger and less-textured struts [7]), the calculated dislocation effect ranges between 100 MPa and 117 MPa. At least two reasons explain why we considered the dislocation density at the core of solidification cells: (1) a 2.10^{15} m^{-2} dislocation density would result in a disproportionately large contribution to strengthening, (2) dislocations in as-built L-PBF specimens are not uniformly distributed, but form a network exactly positioned on the inter-cell segregated areas [32]. Consequently, an indirect influence of this dislocation network will be considered in the cell boundary contribution σ_C.

$$\sigma_{dis} = \alpha . M . b . G . {\rho_0}^{1/2} \quad (5)$$

With α = a geometrical constant (0.33 according to Chen et al. [33], M the Taylor factor, b the Burgers vector (0.25 nm), G the shear modulus, and ρ_0 the dislocation density

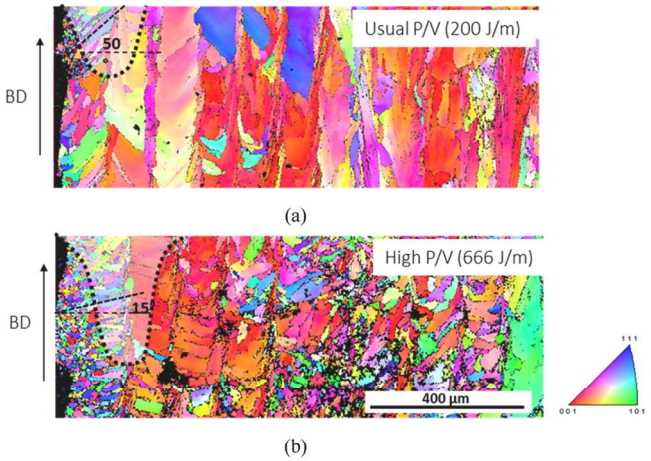

Fig. 25. Influence of lineic energy (J/m) on the orientation of high aspect ratio grains in the external ring of a 2 mm strut and corresponding melt-pool: (a) C_O strategy, (b) 3C_H_O strategy.

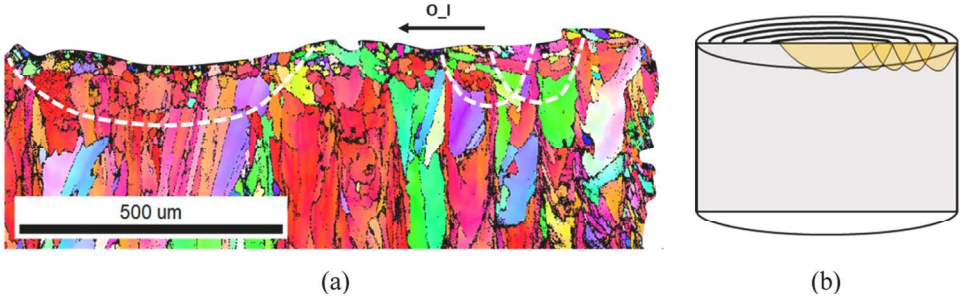

Fig. 24. (a) IPF map of a longitudinal cross-section of the top of a 2 mm strut (C_O strategy) and (b) a diagram showing the superposition of melt pools corresponding to the strategy. A large fusion zone is observed at the center of the strut.

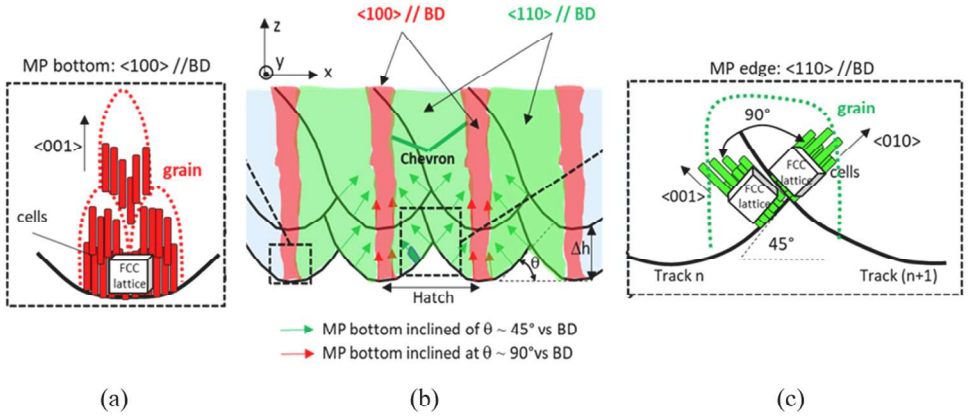

Fig. 26. Diagrams of microstructural selection for vertically aligned L-PBF tracks stacked on top of each other, parallel to the build direction (MP = melt pool): (a) formation of microstructures at the bottom of the melt pool (b), formation of a mixed texture consisting of < 001 > and < 110 > fibers and (c) formation of microstructures from the inclined edges of the melt pool.

Table 3
Solid solution strengthening: k_i constants for Inconel 625 (from Roth et al. [30]).

Elément	Cr	Mo	Nb/Ta	Fe	Al	Ti
wt% / at%	22/ 25.4	9.2/ 5.5	3.7/ 2.5	0.3/ 0.33	0.17/ 0.4	0.14/ 0.25
k_i	337	1015	1183	153	225	775

- Contribution of grain boundaries

According to the Hall-Petch equation (Eq.6), a decrease in grain diameter increases the volume fraction of grain boundaries, and inhibits dislocation motion, thus provoking strengthening. However, one open question in L-PBF alloys concerns the actual contribution of a small number of highly disoriented grains (> 15°) compared to the influence of a large number of low disoriented solidification cells or dendrites (~ 1°) [34]. When considering the obtained grain diameters, and their variation with process parameters and strut size, the grain boundary contribution ranges between 80 and 140 MPa.

$$\sigma_G = k_{y,G} \quad D_g^{-1/2} \tag{6}$$

With $k_{y,G}$ = the Hall-Petch strengthening constant = 750 MPa.μm$^{1/2}$ [35] and D_g: average grain diameter (Fig. 12b).

- Contribution of solidification cells

As shown in Fig. 14, solidification cell equivalent diameters are between 0.6 μm and 1.6 μm. Their contribution to strengthening was also considered through the following formulation proposed by Feaugas [36] who considered the average distance between two non-work-hardened zones, assimilated by Joshi et al. [31] to the inter-cell distance D_c. Such a contribution ranges between 83 MPa (for the smaller diameters) and 183 MPa (for the larger ones) and is clearly differentiating.

$$\sigma_C = f_g \, K_s \, G \, \alpha \, b \, D_c^{-1} \tag{7}$$

With: f_g = average fraction of cells having a non-work-hardened zone (= 1), K_s = constant dependent on the stacking fault energy (SFE) = 2 for low SFE materials like 316 L and Inconel 625, G, α, b indicated in Eq. 5

- Combination of strength contributions

The comparison between calculated strength contributions and experimental yield stresses is depicted in Fig. 27 for the 3C_H_O strategy. The main conclusion to draw from this comparison is that the sum of calculated contributions strongly overestimates experimental data for the smaller strut diameter. One possible explanation is that the < 001 > texture is not adequately accounted in the strengthening models. Conversely, for larger diameters (Fig. 28), the influence of the build strategy is more accurately represented by the sum of analytical expressions of strengthening mechanisms.

5. Conclusion

In this work, vertical Inconel 625 struts of 0.2 mm to 2 mm diameter have been manufactured by L-PBF with various build strategies, but the same laser irradiance (P = 90 W – V = 0.45 m/s). Geometries, microstructures, and tensile properties were thoroughly investigated and the main following conclusions can be drawn:

1. Satisfactory geometries and build accuracy are obtained, with a maximum deviation of + 11 % on build diameters for the smaller struts, and roundness systematically superior to 0.92, tending to increase with strut diameter.
2. Porosity is less than 0.5 %, except for the 3C_H_O outside-in strategy, and the 0.2 mm strut.
3. Regardless of the build strategy, microstructures exhibit a < 001 > //BD fiber texture for D < 0.5 mm, and weaker textures for larger struts. Such a < 001 > texture was initiated by the

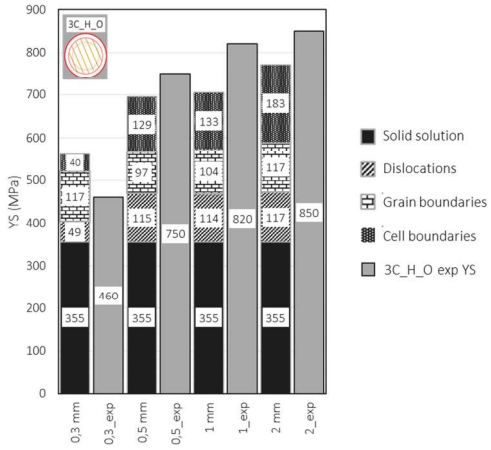

Fig. 27. Sum of calculated strength contributions and comparison with experimental yield strength for 0.3 mm to 2 mm struts (3C_H_O strategy). The solid solution contribution remains constant, while the contributions from cell boundaries and dislocation strengthening account for the lower yield strength observed in the smaller struts.

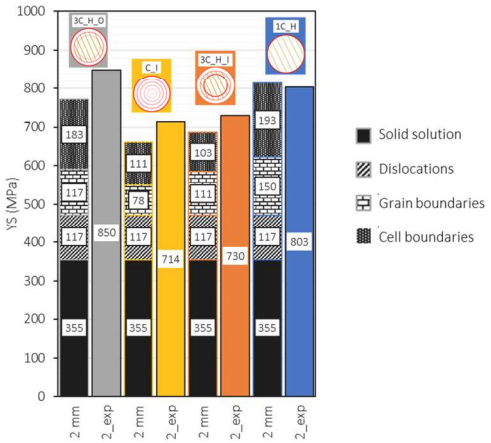

Fig. 28. Comparison between calculated and experimentally determined yield strength for various build strategies (2 mm diameter). The contribution of cell boundaries is the most significant factor in explaining the higher yield observed for the Outside-In strategies.

superposition of a single circular melt pool occupying the whole strut surface for D= 0.2 mm and 0.3 mm. The low curvature solidification front obtained with small diameters explains such a $< 001 >$ preferred orientation.

4. Grain diameters are smaller in the hatching area than in the contour areas. This was explained by a stronger lateral and vertical epitaxy in contour areas.
5. The average diameter of intra-grain solidification cells decreases with strut diameter, and with outside-in strategies.
6. The dislocation density of as-built specimens, estimated between 10^{15} and 2.10^{15} m^{-2} depending on the determination method, does not vary with scan strategy and strut diameter.
7. Higher hardness and better tensile strength are obtained for struts above 0.3 mm diameter, and 1C_H and 3C_H_O strategies. The $< 001 >$ orientation and larger solidification cells for D= 0.3 mm explained the obtained results, affirming the influence of both strut size and scan strategy on microstructures and resulting properties.

All this information offers valuable insights into the manufacturability and engineering of lattice structures primarily composed of small L-PBF struts.

CRediT authorship contribution statement

Zehoua Hamouche: Visualization, Validation, Supervision, Investigation, Data curation. **Julien RODRIGUES DA SILVA**: Writing – review & editing, Writing – original draft, Methodology, Investigation, Formal analysis, Data curation, Conceptualization. **Thierry Baudin**: Visualization, Validation, Supervision, Conceptualization. **Anne-Laure Helbert**: Writing – review & editing, Visualization, Conceptualization. **Patrice Peyre**: Writing – review & editing, Writing – original draft, Visualization, Validation, Supervision, Investigation, Funding acquisition, Conceptualization. **Fréderic Coste**: Software, Resources, Formal analysis.

Declaration of Competing Interest

The authors declare that they have no known competing financial interests or personal relationships that could have appeared to influence the work reported in this paper.

Acknowledgments

The current work has been performed in the frame of a 80PRIME PhD grant by french National Research Agency: Centre national de la recherche scientifique (CNRS).

References

[1] De Terris, T., Castelnau, O., Hadjem-Hamouche, Z., Haddadi, H., Michel, V., Peyre, P., 2021. Analysis of as-built microstructures and recrystallization phenomena on inconel 625 alloy obtained via laser powder bed fusion (L-PBF). Metals 11 (4), 619. https://doi.org/10.3390/met11040619.
[2] Kreitcberg, A., Brailovski, V., Turenne, S., 2017. Effect of heat treatment and hot isostatic pressing on the microstructure and mechanical properties of Inconel 625 alloy processed by laser powder bed fusion. Mater. Sci. Eng.: A 689, 1–10. https://doi.org/10.1016/j.msea.2017.02.038.
[3] Marchese, G., et al., 2018. Influence of heat treatments on microstructure evolution and mechanical properties of Inconel 625 processed by laser powder bed fusion. Mater. Sci. Eng.: A 729, 64–75. https://doi.org/10.1016/j.msea.2018.05.044.
[4] Xiong, Y., et al., 2020. Fatigue behavior and osseointegration of porous Ti-6Al-4V scaffolds with dense core for dental application. Mater. Des. 195, 108994. https://doi.org/10.1016/j.matdes.2020.108994.
[5] Scalzo, F., Totis, G., Vaglio, E., Sortino, M., 2021. Experimental study on the high-damping properties of metallic lattice structures obtained from SLM. Precis. Eng. 71, 63–77. https://doi.org/10.1016/j.precisioneng.2021.02.010.
[6] Leicht, A., Klement, U., Hryha, E., 2018. Effect of build geometry on the microstructural development of 316L parts produced by additive manufacturing. Mater. Charact. 143, 137–143. https://doi.org/10.1016/j.matchar.2018.04.040.
[7] Wang, X., Muñiz-Lerma, J.A., Sánchez-Mata, O., Attarian Shandiz, M., Brochu, M., 2018. Microstructure and mechanical properties of stainless steel 316L vertical struts manufactured by laser powder bed fusion process. Mater. Sci. Eng.: A 736, 27–40. https://doi.org/10.1016/j.msea.2018.08.069.
[8] Niendorf, T., Brenne, F., Schaper, M., 2014. Lattice structures manufactured by SLM: on the effect of geometrical dimensions on microstructure evolution during processing. Met. Mater. Trans. B 45 (4), 1181–1185. https://doi.org/10.1007/s11663-014-0086-z.
[9] Carassus, H., et al., 2022. An experimental investigation into influences of build orientation and specimen thickness on quasi-static and dynamic mechanical responses of selective laser melting 316L stainless steel. Mater. Sci. Eng.: A 835, 142683. https://doi.org/10.1016/j.msea.2022.142683.
[10] Leary, M., et al., 2018. Inconel 625 lattice structures manufactured by selective laser melting (SLM): mechanical properties, deformation and failure modes. Mater. Des. 157, 179–199. https://doi.org/10.1016/j.matdes.2018.06.010.
[11] Yang, L., et al., 2019. Compression–compression fatigue behaviour of gyroid-type triply periodic minimal surface porous structures fabricated by selective laser melting. Acta Mater. 181, 49–66. https://doi.org/10.1016/j.actamat.2019.09.042.
[12] Promoppatum, P., Taprachareon, K., Chayasombat, B., Tanprayoon, D., 2022. Understanding size-dependent thermal, microstructural, mechanical behaviors of additively manufactured Ti-6Al-4V from experiments and thermo-metallurgical simulation. J. Manuf. Process. 75, 1162–1174. https://doi.org/10.1016/j.jmapro.2022.01.068.
[13] Zhang, L., Shi, X., Li, N., Zhao, L., Chen, W., 2021. Heterogeneities of microstructure and mechanical properties for inconel 718 strut tensile sample fabricated by selective laser melting. J. Mater. Res. Technol. 12, 2396–2406. https://doi.org/10.1016/j.jmrt.2021.04.029.
[14] Wróbel, R., Scheel, P., Maeder, X., Hosseini, E., Leinenbach, C., 2023. Microstructure formation in micron-scale thin-walled Hastelloy X samples fabricated with laser powder bed fusion. Prog. Addit. Manuf. https://doi.org/10.1007/s40964-023-00458-z.
[15] Sanchez-Mata, O., Wang, X., Muñiz-Lerma, J.A., Atabay, S.E., Attarian Shandiz, M., Brochu, M., 2022. Characterization of the microstructure and mechanical properties of highly textured and single crystal Hastelloy X thin struts fabricated by laser powder bed fusion. J. Alloy. Compd. 901, 163465. https://doi.org/10.1016/j.jallcom.2021.163465.
[16] Chniouel, A., et al., 2020. Influence of substrate temperature on microstructural and mechanical properties of 316L stainless steel consolidated by laser powder bed fusion. Int J. Adv. Manuf. Technol. 111 (11–12), 3489–3503. https://doi.org/10.1007/s00170-020-06316-4.
[17] Bertsch, K.M., Meric De Bellefon, G., Kuehl, B., Thoma, D.J., 2020. Origin of dislocation structures in an additively manufactured austenitic stainless steel 316L. Acta Mater. 199, 19–33. https://doi.org/10.1016/j.actamat.2020.07.063.
[18] Williamson, G.K., Hall, W.H., 1953. X-ray line broadening from filed aluminium and wolfram. Acta Metall. 1 (1), 22–31. https://doi.org/10.1016/0001-6160(53)90006-6.
[19] Matthews, M.J., Guss, G., Khairallah, S.A., Rubenchik, A.M., Depond, P.J., King, W. E., 2016. Denudation of metal powder layers in laser powder bed fusion processes. Acta Mater. 114, 33–42. https://doi.org/10.1016/j.actamat.2016.05.017.
[20] Zhang, S., Lane, B., Whiting, J., Chou, K., 2019. On thermal properties of metallic powder in laser powder bed fusion additive manufacturing. J. Manuf. Process. 47, 382–392. https://doi.org/10.1016/j.jmapro.2019.09.012.
[21] Li, S., Wei, Q., Shi, Y., Zhu, Z., Zhang, D., 2015. Microstructure characteristics of inconel 625 superalloy manufactured by selective laser melting. Art. no. 9 J. Mater. Sci. Technol. 31 (9). https://doi.org/10.1016/j.jmst.2014.09.020.
[22] Williamson, G.K., Smallman, R.E., 1956. III. Dislocation densities in some annealed and cold-worked metals from measurements on the X-ray debye-scherrer spectrum. Philos. Mag. 1 (1), 34–46. https://doi.org/10.1080/14786435608238074.
[23] Nguejio, J., Szmytka, F., Hallais, S., Tanguy, A., Nardone, S., Godino Martinez, M., 2019. Comparison of microstructure features and mechanical properties for

additive manufactured and wrought nickel alloys 625. Mater. Sci. Eng.: A 764, 138214. https://doi.org/10.1016/j.msea.2019.138214.
[24] Liang, L., et al., 2021. Effect of welding thermal treatment on the microstructure and mechanical properties of nickel-based superalloy fabricated by selective laser melting. Mater. Sci. Eng.: A 819, 141507. https://doi.org/10.1016/j.msea.2021.141507.
[25] Crussard, Ch, Jaoul, B., 1950. Contribution à l'étude de la forme des courbes de traction des métaux et à son interprétation physique. Rev. Met. Paris 47 (8), 589–600. https://doi.org/10.1051/metal/195047080589.
[26] Peyre, P., 2024. Size and build strategy effects for the L-PBF process applied to Inconel 625 vertical struts: a combined numerical and experimental approach (vol. Under Review). Int. J. Adv. Manuf. Tech. (vol. Under Review).
[27] Sofinowski, K.A., Raman, S., Wang, X., Gaskey, B., Seita, M., 2021. Layer-wise engineering of grain orientation (LEGO) in laser powder bed fusion of stainless steel 316L. Addit. Manuf. 38, 101809. https://doi.org/10.1016/j.addma.2020.101809.
[28] Chang, K.-C., et al., 2021. An effective strengthening strategy of nano carbide precipitation and cellular microstructure refinement in a superalloy fabricated by selective laser melting process. Metals 11 (11), 1691. https://doi.org/10.3390/met11111691.
[29] Gypen, L.A., Deruyttere, A., 1977. Multi-component solid solution hardening: part 1 proposed model. J. Mater. Sci. 12 (5), 1028–1033. https://doi.org/10.1007/BF00540987.
[30] Roth, H.A., Davis, C.L., Thomson, R.C., 1997. Modeling solid solution strengthening in nickel alloys. Met. Mater. Trans. A 28 (6), 1329–1335. https://doi.org/10.1007/s11661-997-0268-2.
[31] Joshi, S.S., Keller, C., Mas, L., Lefebvre, W., Hug, E., Couzinie, J.-P., 2023. On the origin of the strain hardening mechanisms of Ni20Cr alloy manufactured by laser powder bed fusion. Int. J. Plast. 165, 103610. https://doi.org/10.1016/j.ijplas.2023.103610.
[32] Wang, G., et al., 2020. The origin of high-density dislocations in additively manufactured metals. Mater. Res. Lett. 8 (8). https://doi.org/10.1080/21663831.2020.1751739. Art. no. 8.
[33] Chen, F., Wang, Q., Zhang, C., Huang, Z., Jia, M., Shen, Q., 2022. Microstructures and mechanical behaviors of additive manufactured Inconel 625 alloys via selective laser melting and laser engineered net shaping. J. Alloy. Compd. 917, 165572. https://doi.org/10.1016/j.jallcom.2022.165572.
[34] Wang, Y., et al., 2021. Hall-Petch relationship in selective laser melting additively manufactured metals: using grain or cell size. J. Cent. South Univ. 28 (4), 1043–1057. https://doi.org/10.1007/s11771-021-4678-x.
[35] Kozar, R.W., Suzuki, A., Milligan, W.W., Schirra, J.J., Savage, M.F., Pollock, T.M., 2009. Strengthening mechanisms in polycrystalline multimodal nickel-base superalloys. Met. Mater. Trans. A 40 (7), 1588–1603. https://doi.org/10.1007/s11661-009-9858-5.
[36] Feaugas, X., 1999. On the origin of the tensile flow stress in the stainless steel AISI 316L at 300 K: back stress and effective stress. Acta Mater. 47 (13), 3617–3632. https://doi.org/10.1016/S1359-6454(99)00222-0.